IEEE Access
Multidisciplinary | Rapid Review | Open Access Journal

Received April 11, 2021, accepted April 21, 2021, date of publication April 23, 2021, date of current version May 3, 2021.

Digital Object Identifier 10.1109/ACCESS.2021.3075388

Field Experiment of Photonic Radar for Low-RCS Target Detection and High-Resolution Image Acquisition

YOUNGSEOK BAE[1], (Student Member, IEEE), JINWOO SHIN[1], (Member, IEEE), SANG-GUG LEE[2], (Senior Member, IEEE), AND HOON KIM[2], (Senior Member, IEEE)

[1]Quantum Physics Technology Directorate, Agency for Defense Development, Daejeon 34186, South Korea
[2]School of Electrical Engineering, Korea Advanced Institute of Science and Technology, Daejeon 34141, South Korea

Corresponding author: Hoon Kim (hoonkim@kaist.ac.kr)

This work was supported by the Agency for Defense Development.

ABSTRACT A photonic radar has recently received considerable interest as a next-generation radar due to its capability to generate wideband signals beyond the technical limitations of the conventional radar. In this paper, we design and implement an *X*-band photonic radar for a low radar cross-section (RCS) target detection and high-resolution image acquisition in real-time. The implemented photonic radar utilizes the photonic frequency quadrupling for the transmitter and detects the dechirped signal by using a delay interferometer and a balanced photo-detector to improve the signal-to-noise ratio. The performance of the photonic radar is verified using a commercial hexacopter having a diagonal wheelbase of 1133 mm as a low-RCS target in the field experiments. We show that the implemented photonic radar can successfully detect the drone on the move even though it is 2.7 km away from the radar. In addition, a high-resolution image of the drone, which is far away 1.1 km from the radar, can be obtained in real-time.

INDEX TERMS Photonic radar, field experiment, low-RCS target detection, high-resolution image acquisition.

I. INTRODUCTION

Recently, as the technology of drones and unmanned aerial vehicles (UAVs) has advanced, the size of drones and UAVs has decreased, and the payload weight, flight speed, and flying distance have increased significantly [1]–[4]. Such technical advances in drones and UAVs are beneficial to the fields of transportation, aerial photography, and rescue, but at the same time, a drone attack including drone strike and drone bombing has also emerged as a threat [5]–[7]. To prevent the drone attack, it is absolutely necessary to detect drones and identify the existence of hazards in advance. However, since the bodies of drones and UAVs could be relatively small and are made of carbon material for weight reduction, the radar cross-section (RCS) is also small [8]. It is very challenging to detect such a low-RCS object with a conventional radar. Even though objects could be detected, it is even more challenging to acquire their image to determine if there exist threats from the object.

The associate editor coordinating the review of this manuscript and approving it for publication was Muguang Wang.

The microwave photonics technology, which combines photonics and microwave engineering [9]–[11], has recently attracted attention as a promising solution for a low-RCS target detection and identification [12]. This technology is capable of generating coherent high-frequency and broadband radar signals with the aid of photonics [12]–[17]. There have been substantial efforts to implement radars by using microwave photonics technology for target image acquisition [15]–[21]. For example, in [16], a novel photonic digital-to-analog converter (DAC) was proposed to process a wide bandwidth signal. In [18], a photonic-based broadband phased array radar architecture was proposed using the radar structure with dechirping process to obtain a high-resolution target image through digital beamforming. Also, a novel coherent receiver structure was proposed to suppress the image frequencies and other undesired frequency-mixing components in [17]. However, since the previous researches focused on the method for generating high-frequency and wide bandwidth signals, most of the previous researches have been conducted in a well-controlled laboratory environment with non-realistic targets such as corner reflectors [15]–[18].

In field experiments reported in [19] and [20], a large passenger airplane was used as a target for image acquisition and a commercial hexacopter was just 120 m away from the radar, respectively. A high-resolution image of a small UAV having a wingspan of 180 cm is acquired in [21]. However, the target UAV was merely 17 meters away from the radar site in this field experiment.

In this paper, we design and implement a photonic radar system for low-RCS target detection and acquisition of a high-resolution target image. The system employs the photonic frequency quadrapling for the generation of broadband radar signals at the transmitter and dechirps the received signal by photonic frequency down-conversion to relieve the bandwidth burden of analog-to-digital converter (ADC) [15]. In order to improve the signal-to-noise ratio (SNR), we employ a delay interferometer (DI) and a balanced photo-detector (BPD) [22]–[25]. The implemented photonic radar is verified through field experiments using a commercial drone having a diagonal wheelbase of merely ∼1 meter. To the best of my knowledge, it is the first field experiment that the image of a low-RCS target is acquired when the target is located over 1 km away from the radar.

Table 1 shows a comparison with previous research results of target image acquisition experiments. We estimate the RCS of the target from the dimensions provided by the references, assuming that the target has a flat surface.

TABLE 1. Comparison with previous research results of target image acquisition experiments.

	[15]	[16]	[17]	[18]	[19]	[20]		[21]	This work
Range (m)	2.35	0.85	2	2.1	800	1200	120	17	**1100**
Bandwidth (GHz)	8	8	8	4	0.6	10		8	**2**
Center freq. (GHz)	22	93	22	24	14.6	35		22	**10**
RCS (m^2)*	6.26	2.52	1.27	0.014	70§	100†	0.01‡	0.01‡	**0.035**¶
FoM (dB)	143.21	142.02	147.34	165.51	219.20	244.51		205.55	**259.68**

* It is estimated from the dimension of the target reported in the reference.
† Target is Boeing-747. The RCS is measured at *X*-band [26].
‡ Target is a commercial drone. The RCS is estimated from [27].
§ Target is Boeing-737. The RCS is measured at *X*-band [28].
¶ It is estimated from the field experiment result.

The radar equation is given by [28]

$$R_{\max}^4 = \frac{P_t G^2 \sigma \lambda^2}{(4\pi)^3\, kTBF(S/N)_{\min}}, \tag{1}$$

where $R_{\max}$ is the maximum detectable range, P_t is the transmit power, G is the antenna gain, σ is the target RCS, λ is the wavelength, k is the Boltzmann's constant, T is the temperature, B is the bandwidth, F is the noise figure of the radar receiver, and $(S/N)_{\min}$ is the minimum SNR. Therefore, the figure of merit (FoM) of the radar system can be defined as [29]

$$\text{FoM (dB)} = 10\log_{10}\left(\frac{R_{\max}^4 B}{\lambda^2 \sigma}\right). \tag{2}$$

Table 1 clearly shows that our field experimental result reported in this paper exhibits superior FoM performance to previous experimental demonstrations.

The organization of this paper is as follows. Section II represents the operation principles and the system requirements of photonic radar, and the designed radar waveform for the detection and image acquisition of low-RCS target. Section III shows the configuration of the implemented photonic radar system and Section IV describes the field experiment and results. Finally, Section V provides the concluding remarks.

II. DESIGN OF PHOTONIC RADAR

In this section, we cover the principles of the photonic radar we implement and system requirements for low-RCS target detection and image acquisition. We present the system parameters of the radar to satisfy the requirements.

A. PRINCIPLES OF PHOTONIC RADAR

The microwave photonic radar based on dechirping process was introduced in [15] and [19] and has been widely used in numerous studies due to its ability to easily generate a wideband signal [30]–[34].

Figure 1 shows the structure of the photonic radar with a DI and a BPD. The operating principle is presented as follows. An intermediate frequency (IF) signal is injected to a dual-parallel Mach-Zehnder modulator (DPMZM) through a 90° hybrid coupler. The carrier frequency and the bandwidth of the applied IF signal are quadrupled by the DPMZM [35], [36]. The frequency-quadrupled DPMZM's output signal is split into two, one sent to a transmit photo-detector (TxPD) and the other to a phase modulator (PM). The TxPD converts the optical signal into electrical signal, which is then transmitted to air over the antenna.

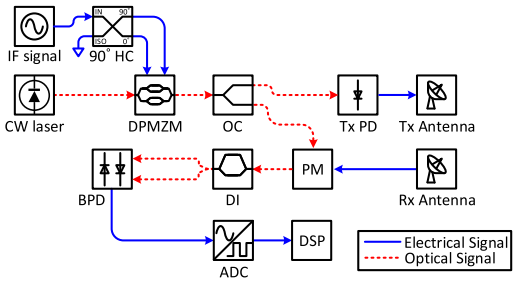

FIGURE 1. Photonic radar using a balanced photo-detector. HC: hybrid coupler, OC: optical coupler, DSP: digital signal processor.

The echo signal received by a receiving antenna is sent to the PM, which modulates the frequency of the DPMZM output signal. This dechirping process relieves the bandwidth burden of ADC [15]. A DI is used to convert the PM signal into an intensity modulation. The use of a BPD doubles signal amplitude and cancels the relative intensity noise (RIN) of the laser source, thus improving the SNR [22]–[25].

The CW laser output can be expressed as

$$E_{\text{CW}}(t) = E_c \cos(\omega_c t), \tag{3}$$

where E_c and ω_c are the amplitude and angular frequency of the CW laser source, respectively. When an IF signal with the

angular frequency of ω_{IF} is applied to the 90° hybrid coupler, the IF signal is split into two with $\pi/2$ phase difference between them. The split RF signals are fed to the children Mach-Zehnder modulators (MZMs) of the DPMZM, which are biased at their maximum transmission. At the same time, the mother MZM of the DPMZM operates at the minimum transmission point to generate the frequency-quadrupled signal. Thus, the output signal of the PM can be written as

$$\begin{aligned} E_{\mathrm{PM}}(t) = & -E_c J_2(m) \\ & \times\Big[J_0(m')\big\{\cos(\omega_c t - 2\omega_{\mathrm{IF}} t) + \cos(\omega_c t + 2\omega_{\mathrm{IF}} t)\big\} \\ & + jJ_1(m')\big\{\cos(\omega_c t + 6\omega_{\mathrm{IF}} t + \alpha) \\ & + \cos(\omega_c t - 2\omega_{\mathrm{IF}} t - \alpha) + \cos(\omega_c t + 2\omega_{\mathrm{IF}} t + \alpha) \\ & + \cos(\omega_c t - 6\omega_{\mathrm{IF}} t - \alpha)\big\}\Big], \end{aligned} \tag{4}$$

where $J_n(\cdot)$ means the n^{th}-order Bessel function of the first kind, $\alpha = 8\pi k \Delta\tau t$ is the angular frequency caused by the time delay ($\Delta\tau$) due to target reflection, k is the chirp rate of the IF signal, and m and m' are the modulation indices of the DPMZM and the PM, respectively.

If the DI splits the input signal equally, the output signals of the DI is [37]

$$\begin{aligned} E_{\mathrm{DI},1}(t) &= -\exp(-j\phi_0)\sin\left(\frac{\Delta\phi}{2}\right) E_{\mathrm{PM}}(t), \text{ and} \\ E_{\mathrm{DI},2}(t) &= j\exp(-j\phi_0)\cos\left(\frac{\Delta\phi}{2}\right) E_{\mathrm{PM}}(t), \end{aligned} \tag{5}$$

where ϕ_0 is the average phase delay and $\Delta\phi$ is the differential phase shift of the DI. Since $\Delta\phi$ is $\pi/2$, the output current of each photo-detector of the BPD with responsivity, $\Re$, can be written as

$$\begin{aligned} I_{\mathrm{BPD},1}(t) = & \frac{\Re E_c^2 J_2^2(m)}{2} \\ & + (\Re/8)\Big[E_c^2 J_2^2(m)\big\{4(J_0^2(m') + 2\,J_1^2(m')) \\ & + 4\,J_1^2(m')\cos(4\omega_{\mathrm{IF}} t + 16\pi k \Delta\tau t) \\ & + 8\,J_1^2(m')\cos(4\omega_{\mathrm{IF}} t) \\ & + 4\,J_0^2(m')\cos(4\omega_{\mathrm{IF}} t)\big\}\Big], \text{ and} \\ I_{\mathrm{BPD},2}(t) = & \frac{\Re E_c^2 J_2^2(m)}{2} \\ & - (\Re/8)\Big[E_c^2 J_2^2(m)\big\{4(J_0^2(m') + 2\,J_1^2(m')) \\ & + 4\,J_1^2(m')\cos(4\omega_{\mathrm{IF}} t + 16\pi k \Delta\tau t) \\ & + 8\,J_1^2(m')\cos(4\omega_{\mathrm{IF}} t) \\ & + 4\,J_0^2(m')\cos(4\omega_{\mathrm{IF}} t)\big\}\Big]. \end{aligned} \tag{6}$$

Therefore, the differential current of the BPD is

$$\begin{aligned} \Delta I_{\mathrm{BPD}}(t) &= I_{\mathrm{BPD},2}(t) - I_{\mathrm{BPD},1}(t) \\ &= -\Re\Big[E_c^2 J_2^2(m)\big\{(J_0^2(m') + 2\,J_1^2(m')) \\ &\quad + J_1^2(m')\cos(4\omega_{\mathrm{IF}} t + 16\pi k \Delta\tau t) \\ &\quad + 2\,J_1^2(m')\cos(4\omega_{\mathrm{IF}} t) \\ &\quad + J_0^2(m')\cos(4\omega_{\mathrm{IF}} t)\big\}\Big]. \end{aligned} \tag{7}$$

As shown in Eq. 7, the BPD doubles the photocurrent associated with the beat frequency when compared to Eq. 6. Also, the RIN of the laser source can be suppressed by the common-mode rejection [22]–[25].

B. SYSTEM REQUIREMENTS

Table 2 shows the system requirements of the photonic radar for target detection and image acquisition. The photonic radar has two operation modes: the detection and image acquisition modes. Both operation modes employ the center frequency of 10 GHz since this frequency band is widely used in military applications due to the low atmosphere absorption [38]. The detectable target velocity is set to 72 km/h (= 20 m/s), since we have considered commercial drones having a maximum speed of 60 km/h (= 16.67 m/s) [39].

TABLE 2. System requirements of the photonic radar for target detection and image acquisition.

	Detection mode	Image acquisition mode
Center frequency (f_c)	10 GHz	
Range resolution (ΔR)	30 m	0.1 m
Max. target velocity ($v_{\max}$)	72 km/h	
Max. target range ($R_{\max}$)	5 km	1.1 km

The different requirements between two operation modes are the range resolution and maximum target range. First, the requirement of the range resolution in the detection mode is set to 30 m because the minimum distance between drones would be larger than 50 m when drones fly in swarm formation [40]. In the image acquisition mode, on the other hand, the range resolution is set to 0.1 m since typical commercial micro-drones have a wheelbase length longer than 0.1 meter [41].

Finally, the requirement of the maximum target range is set to 5 km in the detection mode. However, in the image acquisition mode, the maximum target range is set to 1.1 km due to the wider signal bandwidth.

C. RADAR WAVEFORM DESIGN

Table 3 shows the design results of the radar waveform of the photonic radar. The optical delay line of 1 km is used to reduce the maximum beat frequency in the image acquisition mode. Since a long optical delay line might produce a phase shift caused by temperature variation and external vibrations, the long delay line needs to be vibration-isolated and temperature-controlled.

Signal bandwidths are set to 5 MHz and 2 GHz in the detection and the image acquisition modes, respectively. The pulse repetition interval (PRI) is set to 200 μs in both operation modes for design simplicity. The number of coherent

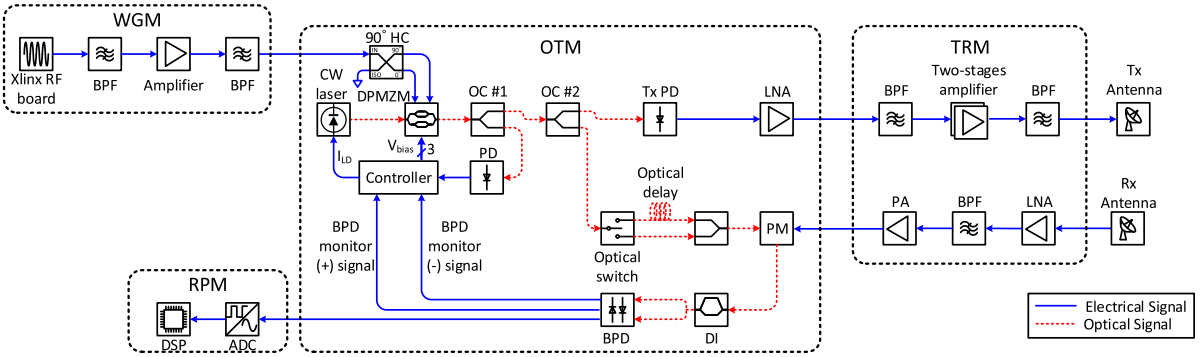

FIGURE 2. The schematic diagram of the implemented photonic radar system. BPF: bandpass filter, PA: power amplifier, LNA: low-noise amplifier.

TABLE 3. Radar waveform design results of the photonic radar for low-RCS target detection and image acquisition.

	Detection mode	Image acquisition mode
Signal bandwidth (B)	5 MHz	2 GHz
Pulse repetition interval (PRI)	200 μs	
Maximum beat frequency (f_{bmax})	833.33 kHz	6.67 MHz
Coherent pulse number (M)	128	
Range bin number (L)	4096	
Apparent range resolution (ΔR_{a})	2.44 m	0.537 m

pulses (M) and the number of range bins (L) are 128 and 4096, respectively, for maximizing the fast Fourier transform (FFT) efficiency in signal processing.

To avoid the range-cell migration occurrence, the apparent range resolution (ΔR_{a}) should be larger than the distance traveled by the target at the maximum velocity over the entire pulse duration (ΔR_{max}). In the detection mode, the maximum distance the target moves during the pulse duration is 0.853 m because ΔR_{max} equals $M \times \mathrm{PRI} \times v_{\mathrm{max}}$. The apparent range resolution in the detection mode is 2.44 m ($= 2R_{\mathrm{max}}/L$). Similarly, in the image acquisition mode, the maximum moving distance is 0.512 m and the apparent range resolution is 0.537 m. Thus, the range-cell migration does not occur in each operation mode.

III. IMPLEMENTATION OF PHOTONIC RADAR

Figure 2 shows the schematic diagram of the implemented photonic radar system. The system consists of four modules: a waveform generation module (WGM), an optical transmit/receive module (OTM), a transmit/receive module (TRM), and a radar signal processing module (RPM). A thermal controller is equipped on the back of our system rack (shown in Fig. 6) to stabilize the temperature. This helps to reduce the performance degradation caused by temperature variations, such as a phase shift in the 1-km long optical delay.

A. WAVEFORM GENERATION MODULE

The WGM, which generates a narrow-band IF signal, is realized by using a Xilinx's ZCU-111 board. The 2.5-GHz IF signal is then amplified to 35 dBm to be fed to OTM. Two bandpass filters are used to improve the extinction ratio of the signal.

Figure 3 shows the electrical spectra of the IF signal generated by WGM. The IF signal is a linearly frequency-modulated up-chirp signal having a PRI of 200 μs. The IF signal has a center frequency of 2.5 GHz. Also, the signal bandwidths are 1.25 and 500 MHz in the detection and image acquisition modes, respectively. These signals are frequency-quadrupled at the OTM.

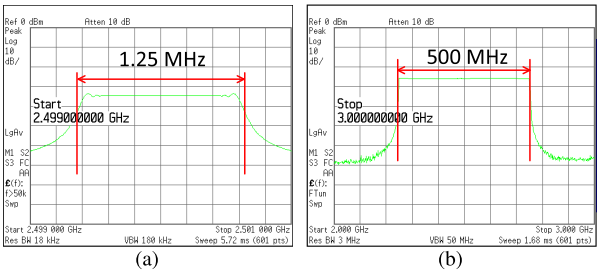

FIGURE 3. The electrical spectra of the IF signal produced by WGM. (a) IF signal with a center frequency of 2.5 GHz and bandwidth of 1.25 MHz for detection mode. (b) IF signal with a center frequency of 2.5 GHz and bandwidth of 500 MHz for image acquisition mode.

B. OPTICAL TRANSMIT/RECEIVE MODULE

The OTM is composed of the optical transmitter and the receiver. In the transmitter of the OTM, the output power of the CW laser is set to 18 dBm at a wavelength of 1550 nm. The IF signal drives the DPMZM through a 90° hybrid coupler. The output signal of the DPMZM is split into two and sent to the TxPD and the PM of the receiver. The signal is converted to the electrical signal by the TxPD and amplified by a low-noise amplifier with a gain of 12 dB. Figure 4 shows the signal spectra measured at the output of low-noise amplifier. The output signal has a center frequency of 10 GHz and the bandwidths of 5 MHz and 2 GHz, respectively. Fig. 3 and Fig. 4 confirm that the output signal of the OTM is frequency-quadrupled with respect to the IF signal.

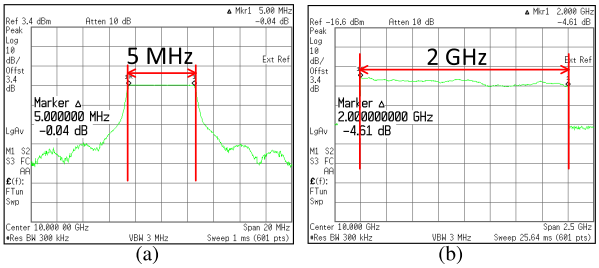

FIGURE 4. The electrical spectra of the frequency-quadrupled signal by OTM. (a) The quadrupled signal with a center frequency of 10 GHz and bandwidth of 5 MHz for detection mode. (a) The quadrupled signal with a center frequency of 10 GHz and bandwidth of 2 GHz for image acquisition mode.

The receiver of the OTM is composed of the PM, an optical delay line, an optical switch, the DI, and the BPD. The output of the DPMZM is sent to the optical switch for the selection of the optical delay line use. Since the PM is polarization-sensitive, we use a polarization-maintaining fiber as the optical delay line. Only in the image acquisition mode, the optical delay line is used to reduce of the beat frequency. The 1-km spooled optical fiber delay is covered with sponge to absorb external vibrations. The switch-passed signal is fed to the PM. The PM modulates the output signal of the DPMZM by the echo signal received by the TRM. The bias points of two children MZMs and mother MZM in the DPMZM are stabilized during the system operation by monitoring the optical powers of two photo-detectors in the BPD.

Figure 5 shows the comparison of the intensity of beat signals in the cases of using the BPD and a single-input photo-detector (SPD). The beat signals are measured in both the cases, and a gain method [42] is used for the signal intensity analysis. For this measurement, we insert a 23-m long optical delay line between the optical coupler (labeled OC #2 in Fig. 2) and TxPD, and then feed the output of TxPD directly to the PM, without using TRM. The noise equivalent bandwidth of both beat signals is measured to be 198.54 kHz. As shown in Fig. 5, the gain of beat frequency is increased by 2.75 dB by using the BPD. Therefore, we have confirmed that the overall photonic radar system performance is improved by employing the DI and the BPD.

C. TRANSMIT/RECEIVE MODULE

The TRM is composed of the RF transmitter and the receiver, which amplifies the transmit signal and receives the echo signal, respectively. The TRM output signal is emitted to air through the transmit antenna having a gain of 35.5 dB.

When the echo signal is received, the receiver amplifies it, and then filters out the out-of-band noise. Finally, the received signal is amplified to the level required by the OTM.

D. RADAR SIGNAL PROCESSING MODULE

The RPM converts the received beat signal from the analog domain to the digital domain through the ADC and performs the signal processing to extract information of the target in real-time. For this purpose, the radar signal processing procedures are composed of two FFTs. Since the first

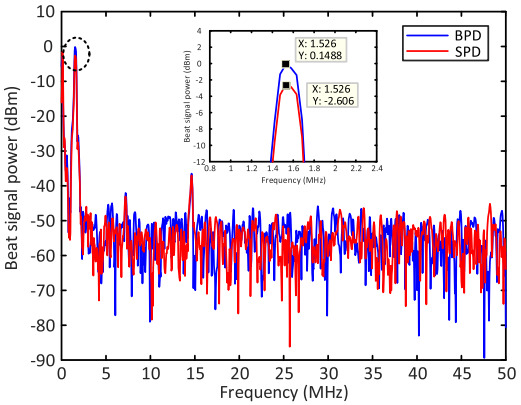

FIGURE 5. The electrical spectra of the beat signal when either a BPD or a SPD is used after the DI.

FFT determines the range of the target, it is generally called the range FFT [43]. The frequency shift is proportional to the distance between the antenna and the target. Therefore, when the range FFT of all chirps of the radar signal has been performed, the relative velocity of the target can be determined by performing the Doppler FFT using the results of the range FFT. The relative velocity of the target can be obtained by a phase shift from the range bin of pulse to the range bin of the next pulse, which represents the Doppler frequency. The results of the Doppler FFT are processed through a constant false alarm rate (CFAR) algorithm which sets a threshold value according to the ambient noise to detect the target [44]. As a result, real-time signal processing has been realized in the RPM.

IV. FIELD EXPERIMENTS AND RESULTS

Figure 6 shows the implemented photonic radar. In this Section, we describe scenarios for field experiments and show the results of field experiments under each operation mode.

FIGURE 6. The implemented photonic radar for low-RCS target detection and image acquisition.

A. FIELD EXPERIMENT

Figure 7 shows the photo of the implemented photonic radar. For the field experiment, a commercial hexacopter

FIGURE 7. A photo taken during the field experiment.

(DJI Inc., Matrice 600), which has a diagonal wheelbase of 1133 mm, is used as a low-RCS target. Figure 8 shows the field experiment scenario using the drone. The scenario starts with the drone moving up 500 m above the point at a distance of 1 km from the antenna. We denote the initial location of the drone as Point 1, as shown in Fig. 8. From Point 1, the drone flies at a speed of 10 m/s to Point 3, which is 2.6 km away from the antenna, via Point 2 at a distance of 1.7 km from the antenna while maintaining its altitude. When the drone arrives at Point 3, the drone hovers at the location for 30 seconds and flies back to Point 1 via Point 2 with a velocity of 10 m/s. When the drone arrives at Point 1, the drone starts hovering for 5 minutes. The field experiment scenario is finished when the drone lands on the ground.

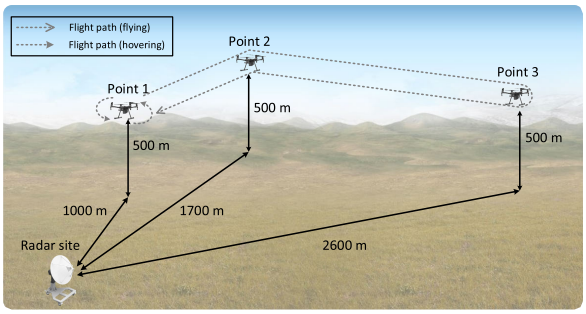

FIGURE 8. The field experiment scenario of the implemented photonic radar.

B. TARGET DETECTION

During the field experiment, a lot of clutters are simultaneously received together with the echo signals from the target. Most of clutters can be eliminated through the CFAR algorithm [44]. Figure 9 shows the range-Doppler map after CFAR algorithm of the field experiment results. In Fig. 9,

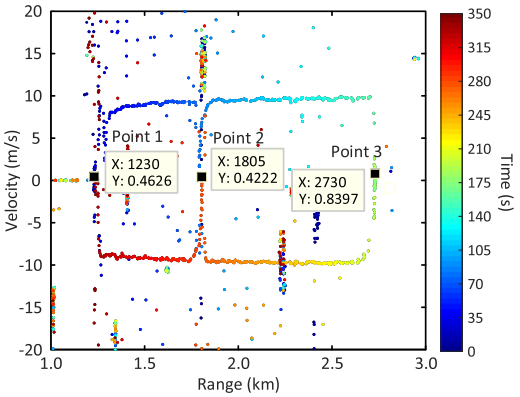

FIGURE 9. The range-Doppler map of the field experiment results in the detection mode.

the color of dots is changed from blue to red in order of data received time. The negative sign of the velocity means that the flying direction of the drone heads towards the radar site. The detected drone moves between 1200 and 2700 m with a fairly uniform velocity except the points where the drone changes the direction. The signal produced by the clouds also exhibits a Doppler frequency shift [45]. Clouds are founded at 1, 1.8, 2.3, and 2.4 km away from the antenna.

Figure 10 shows the signal magnitude as a function of range. The blue-cross marks refer to the range FFT data through the field experiment. The black-dotted line and the red-solid line are the theoretical line of the measured data based on the radar equation [43] and the minimum detectable signal level of the range FFT data, respectively. According to the CFAR-processed data, the noise floor is measured to be -90 dBm/Hz. Since the minimum SNR for signal processing is designed to 13 dB, the minimum detectable signal level is determined to be -77 dBm. Because the RCS of the drone could fluctuate by the orientation, the magnitude of the measured data shown in Fig. 10 can vary even at the same distance. Based on the measured data, the RCS of the drone used in the field experiment is estimated in the range of 0.035 m^2 (-14.56 dBsm) and 0.12 m^2 (-9.21 dBsm). In Fig. 10, we draw a line for signal magnitude estimated from the radar equation, assuming that the RCS of the drone is 0.035 m^2. Although the theoretical curve is obtained by using the smallest RCS value estimated from the measurement, the maximum target range is estimated to be longer than 5 km. Therefore, the requirement of the maximum detection range presented in Section II of the implemented photonic radar is satisfied.

C. IMAGE ACQUISITION

To acquire the target image, the RPM performs range FFT and obtain a high-resolution range profile for each range in real-time [46]. We use the average range profile algorithm to compensate for the fluctuation of the distance component [47]. In addition, the phase correction is performed using the maximum constant phase adjustment algorithm in order to compensate for the phase component fluctuations occurring when the target moves [48].

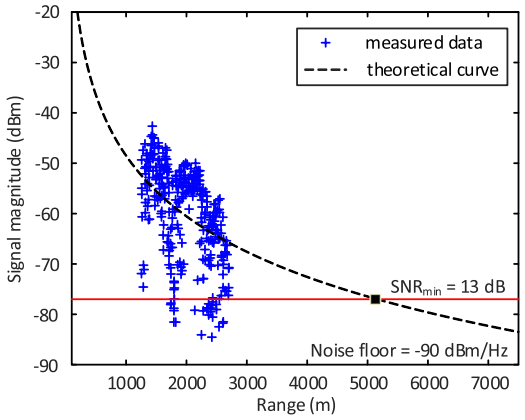

FIGURE 10. The estimation of the maximum detectable range of the implemented photonic radar.

Figure 11 shows the acquired image of the drone hovering at 1.1 km from the radar site (i.e., Point 1). Since the signal bandwidth is 2 GHz in the image acquisition mode, the theoretical resolution is 0.075 m. The six blades of hexacopter are identified in Fig. 11. Therefore, it is verified that the implemented photonic radar obtains the low-RCS target image successfully.

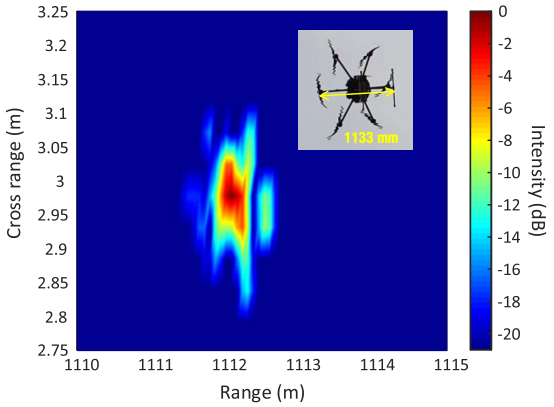

FIGURE 11. The acquired image of the drone hovering at 1.1 km.

V. CONCLUSION

In this paper, we design and implement a radar system for low-RCS target detection and image acquisition using photonic frequency quadrupling and dechirping. The performance of the implemented radar system is verified through the field experiment using a drone having an RCS of 0.035 m^2. An optical delay interferometer and a balanced photo-detector are used to improve the SNR in this radar system. Our field experiment results show that the photonic radar can detect the drone on the move as far as 2.7 km away from the radar site in the target detection mode. In addition, the maximum detectable range of the radar is estimated to be >5 km from the radar site. Also, a clear image of the low-RCS drone is captured in the image acquisition mode when the drone hovers at 1.1 km away from the radar site. For example, the six arms of the drone are clearly identified.

We believe that the photonic radar can be an alternative to the traditional radar for low-RCS target surveillance and can be adopted as a promising candidate for a software-defined radar in the future.

REFERENCES

[1] J. M. Martínez-Heredia, F. Colodro, J. L. Mora-Jiménez, A. Remujo, J. Soriano, and S. Esteban, "Development of GaN technology-based DC/DC converter for hybrid UAV," *IEEE Access*, vol. 8, pp. 88014–88025, 2020.

[2] S. Jordan, J. Moore, S. Hovet, J. Box, J. Perry, K. Kirsche, D. Lewis, and Z. T. H. Tse, "State-of-the-art technologies for UAV inspections," *IET Radar, Sonar Navigat.*, vol. 12, no. 2, pp. 151–164, Feb. 2018.

[3] C. Kyrkou and T. Theocharides, "EmergencyNet: Efficient aerial image classification for drone-based emergency monitoring using atrous convolutional feature fusion," *IEEE J. Sel. Topics Appl. Earth Observ. Remote Sens.*, vol. 13, pp. 1687–1699, 2020.

[4] K. J. Wu, T. S. Gregory, J. Moore, B. Hooper, D. Lewis, and Z. T. H. Tse, "Development of an indoor guidance system for unmanned aerial vehicles with power industry applications," *IET Radar, Sonar Navigat.*, vol. 11, no. 1, pp. 212–218, 2016.

[5] D. Walsh and I. T. Mehsud, *Civilian Deaths in Drone Strikes Cited in Report*. New York, NY, USA: The NewYork Times, 2013, Accessed: Oct. 22, 2013. [Online]. Available: https://www.nytimes.com

[6] B. Hubbard, P. Karasz, and S. Reed, *Two Major Saudi Oil Installations Hit by Drone Strike, and U.S. Blames Iran*. New York, NY, USA: The NewYork Times, 2019. Accessed: Sep. 14, 2019. [Online]. Available: https://www.nytimes.com

[7] D. M. Halbfinger, *Israel Says it Struck Iranian killer Drone Sites in Syria*. New York, NY, USA: The NewYork Times, 2019. Accessed: Sep. 14, 2019. [Online]. Available: https://www.nytimes.com

[8] S. Rahman and D. A. Robertson, "In-flight RCS measurements of drones and birds at K-band and W-band," *IET Radar, Sonar Navigat.*, vol. 13, no. 2, pp. 300–309, 2018.

[9] J. Francoy, S. S. Maicas, I. G. Mestre, J. M. Almerich, J. L. Soler, and J. S. Durá, "Innovative concepts in microwave photonics," *Waves*, vol. 4, pp. 43–58, 2012.

[10] S. Iezekiel, M. Burla, J. Klamkin, D. Marpaung, and J. Capmany, "RF engineering meets optoelectronics: Progress in integrated microwave photonics," *IEEE Microw. Mag.*, vol. 16, no. 8, pp. 28–45, Dec. 2015.

[11] J. Capmany and D. Novak, "Microwave photonics combines two worlds," *Nature Photon.*, vol. 1, no. 6, pp. 319–330, Apr. 2007.

[12] S. Pan and Y. Zhang, "Microwave photonic radars," *J. Lightw. Technol.*, vol. 38, no. 19, pp. 5450–5484, 2020.

[13] R. W. Ridgway, C. L. Dohrman, and J. A. Conway, "Microwave photonics programs at DARPA," *J. Lightw. Technol.*, vol. 32, no. 20, pp. 3428–3439, Oct. 15, 2014.

[14] P. Ghelfi, "A fully photonics-based coherent radar system," *Nature*, vol. 507, no. 7492, pp. 341–345, Mar. 2014.

[15] F. Zhang, Q. Guo, Z. Wang, P. Zhou, G. Zhang, J. Sun, and S. Pan, "Photonics-based broadband radar for high-resolution and real-time inverse synthetic aperture imaging," *Opt. Exp.*, vol. 25, no. 14, pp. 16274–16281, 2017.

[16] S. Peng, S. Li, X. Xue, X. Xiao, D. Wu, X. Zheng, and B. Zhou, "High-resolution W-band ISAR imaging system utilizing a logic-operation-based photonic digital-to-analog converter," *Opt. Exp.*, vol. 26, no. 2, pp. 1978–1987, 2018.

[17] X. Ye, F. Zhang, Y. Yang, and S. Pan, "Photonics-based radar with balanced I/Q de-chirping for interference-suppressed high-resolution detection and imaging," *Photon. Res.*, vol. 7, no. 3, pp. 265–272, 2019.

[18] B. Gao, F. Zhang, E. Zhao, D. Zhang, and S. Pan, "High-resolution phased array radar imaging by photonics-based broadband digital beamforming," *Opt. Exp.*, vol. 27, no. 9, pp. 13194–13203, 2019.

[19] R. Li, "Demonstration of a microwave photonic synthetic aperture radar based on photonic-assisted signal generation and stretch processing," *Opt. Exp.*, vol. 25, no. 13, pp. 14334–14340, 2017.

[20] A. Wang, J. Wo, X. Luo, Y. Wang, W. Cong, P. Du, J. Zhang, B. Zhao, J. Zhang, Y. Zhu, J. Lan, and L. Yu, "Ka-band microwave photonic ultra-wideband imaging radar for capturing quantitative target information," *Opt. Exp.*, vol. 26, no. 16, pp. 20708–20717, 2018.

[21] F. Zhang, Q. Guo, Y. Zhang, Y. Yao, P. Zhou, D. Zhu, and S. Pan, "Photonics-based real-time and high-resolution ISAR imaging of non-cooperative target," *Chin. Opt. Lett.*, vol. 15, no. 11, 2017, Art. no. 112801.
[22] G. Abbas, V. Chan, and T. Yee, "A dual-detector optical heterodyne receiver for local oscillator noise suppression," *J. Lightw. Technol.*, vol. 3, no. 5, pp. 1110–1122, Oct. 1985.
[23] M. Abtahi, S. Ayotte, J. Penon, and L. A. Rusch, "Balanced detection of correlated incoherent signals: A statistical analysis of intensity noise with experimental validation," *J. Lightw. Technol.*, vol. 26, no. 10, pp. 1330–1338, May 2008.
[24] C. B. Albert, C. Huang, and E. Hoi Wing Chan, "Intensity noise suppression using dual-polarization dual-parallel modulator and balanced detector," *IEEE Photon. J.*, vol. 10, no. 2, pp. 1–8, Apr. 2018.
[25] Y. Painchaud, M. Poulin, M. Morin, and M. Têtu, "Performance of balanced detection in a coherent receiver," *Opt. Exp.*, vol. 17, no. 5, pp. 3659–3672, 2009.
[26] A. David, C. Brousseau, and A. Bourdillon, "Simulations and measurements of a radar cross section of a Boeing 747–200 in the 20–60 MHz frequency band," *Radio Sci.*, vol. 38, no. 4, pp. 3-1–3-4, 2003.
[27] Á. D. De Quevedo, F. I. Urzaiz, J. G. Menoyo, and A. A. López, "Drone detection and RCS measurements with ubiquitous radar," in *Proc. Int. Conf. Radar (RADAR)*, Aug. 2018, pp. 1–6.
[28] M. I. Skolnik, *Radar Handbook*. New York, NY, USA: McGraw-Hill, 2008.
[29] G. G. Silberman, "Millimeter wave front-end figure of merit. Part 1," U.S. ARMY Armament Res. Develop. Eng. Center, Picatinny Arsenal, NJ, USA, Tech. Rep. ARFSD-TR-93046, Apr. 1994.
[30] F. Zhang, B. Gao, and S. Pan, "Photonics-based MIMO radar with high-resolution and fast detection capability," *Opt. Exp.*, vol. 26, no. 13, pp. 17529–17540, 2018.
[31] J. Shi, F. Zhang, D. Ben, and S. Pan, "Simultaneous radar detection and frequency measurement by broadband microwave photonic processing," *J. Lightw. Technol.*, vol. 38, no. 8, pp. 2171–2179, 2020.
[32] R. Cheng, W. Wei, W. Xie, and Y. Dong, "Photonic generation of programmable coherent linear frequency modulated signal and its application in X-band radar system," *Opt. Exp.*, vol. 27, no. 26, pp. 37469–37480, 2019.
[33] Y. Bae, M. Yi, J. Shin, and S.-G. Lee, "X-band photonic-based pulsed radar architecture with a high range resolution," *Appl. Sci.*, vol. 10, no. 18, p. 6558, 2020.
[34] R. Li, W. Li, Y. Dong, B. Wang, Z. Wen, Y. Luan, Z. Yang, X. Yang, J. Yang, W. Sun, L. Chen, Z. Mo, C. Liu, J. Dong, H. Zeng, and Z. Yin, "An ultrahigh-resolution continuous wave synthetic aperture radar with photonic-assisted signal generation and dechirp processing," in *Proc. 17th Eur. Radar Conf. (EuRAD)*, Oct. 2021, pp. 13–16.
[35] C.-T. Lin, P.-T. Shih, J. Chen, W.-J. Jiang, S.-P. Dai, P.-C. Peng, Y.-L. Ho, and S. Chi, "Optical millimeter-wave up-conversion employing frequency quadrupling without optical filtering," *IEEE Trans. Microw. Theory Techn.*, vol. 57, no. 8, pp. 2084–2092, Aug. 2009.
[36] Y. Fu, X. Zhang, B. Hraimel, T. Liu, and D. Shen, "Mach-Zehnder: A review of bias control techniques for Mach-Zehnder modulators in photonic analog links," *IEEE Microw. Mag.*, vol. 14, no. 7, pp. 102–107, Nov. 2013.
[37] R. Hui and M. O'Sullivan, *Fiber Optic Measurement Techniques*. New York, NY, USA: Academic, 2009.
[38] C. O. R. P. Editors, "Attenuation by atmospheric gases and related effects," Int. Telecommun. Union-R, Geneva, Switzerland, Tech. Rep. ITU-R P. 676-12, Aug. 2019.
[39] FreeFly Technical Staff. (2020). *ALTA 8 Specifications*. [Online]. Available: https://freeflysystems.com/alta-8/specs
[40] D. Journalist. (Oct. 2018). *Hiring a Drone Operator What You Need to Know About Flying Distance*. [Online]. Available: https://dronesaferegister.org.uk//
[41] Extreme Fliers Technical Staff. (2020). *Micro Drone 4.0 Small, Intelligent, Autonomous*. [Online]. Available: https://www.microdrone.co.uk/
[42] *Fundamentals of RF and Microwave Noise Figure Measurements*, Keysight Technology, Santa Rosa, CA, USA, 2019.
[43] B. R. Mahafza, *Radar Systems Analysis and Design Using MATLAB*. Boca Raton, FL, USA: CRC Press, 2016.
[44] R. Nitzberg, "Constant-false-alarm-rate signal processors for several types of interference," *IEEE Trans. Aerosp. Electron. Syst.*, no. 1, pp. 27–34, 1972.
[45] A. Hasler, W. Shenk, and W. Skillman, "Wind estimates from cloud motions: Phase 1 of an *in situ* aircraft verification experiment," *J. Appl. Meteorol.*, vol. 15, no. 1, pp. 10–15, 1976.
[46] M. C. Edwards, "Design of a continuous-wave synthetic aperture radar system with analog dechirp," M.S. thesis, Dept. Elect. Comput. Eng., Brigham Young Univ., Provo, UT, USA, 2009.
[47] D. Zhu, L. Wang, Y. Yu, Q. Tao, and Z. Zhu, "Robust ISAR range alignment via minimizing the entropy of the average range profile," *IEEE Geosci. Remote Sens. Lett.*, vol. 6, no. 2, pp. 204–208, Apr. 2009.
[48] J. Wang, X. Liu, and Z. Zhou, "Minimum-entropy phase adjustment for ISAR," *IEE Proc.-Radar, Sonar Navigat.*, vol. 151, no. 4, pp. 203–209, Aug. 2004.

YOUNGSEOK BAE (Student Member, IEEE) received the B.S. and M.S. degrees in electrical engineering from Korea University, Seoul, South Korea, in 2009 and 2011, respectively. He is currently pursuing the Ph.D. degree with the Korea Advanced Institute of Science and Technology. Since 2011, he has been a Senior Researcher with the Agency for Defense Development, Daejeon, South Korea. His research interests include photonic analog-to-digital converter, silicon photonics, and microwave photonic radar.

JINWOO SHIN (Member, IEEE) received the B.S., M.S., and Ph.D. degrees in electrical engineering from the University of Seoul, Seoul, South Korea, in 1995, 1997, and 2014, respectively. Since 1997, he has been working as a Principal Researcher with the Agency Defense Development, Daejeon, South Korea. His current research interests include numerical modeling and analysis of active array systems, microwave photonic radar, and wireless power transmission.

SANG-GUG LEE (Senior Member, IEEE) received the B.S. degree in electronic engineering from Kyungbook National University, South Korea, in 1981, and the M.S. and Ph.D. degrees in electrical engineering from the University of Florida, Gainesville, in 1989 and 1992, respectively.

In 1992, he joined Harris Semiconductor, Melbourne, Florida, where he was engaged in silicon-based RFIC designs. From 1995 to 1998, he was an Assistant Professor with the School of Computer and Electrical Engineering, Handong University, Pohang, South Korea. From 1998 to 2009, he was with the Information and Communications University, Daejeon, South Korea, where he become a Full Professor. Since 2009, he has been a Professor with the Department of Electrical Engineering, Korea Advanced Institute of Science and Technology (KAIST), Daejeon. His research interests include CMOS-based RF, analog, mixed mode IC designs for various radio transceivers, especially the ultra-low power applications, high-frequency (THz) circuit designs, display semiconductors, and energy-harvesting IC designs.

HOON KIM (Senior Member, IEEE) is currently an Associate Professor with the School of Electrical Engineering, KAIST. Prior to joining KAIST in 2014, he was with Bell Laboratories, Lucent Technologies, from 2000 to 2001, Samsung Electronics, South Korea, from 2001 to 2007, and National University of Singapore, from 2007 to 2014. His research interests include high-capacity fiber-optic communication systems, free-space optical communications, broadband optical access networks, and photonic systems. He serves as a Senior Editor for *IEEE Photonics Technology Letters* and an Associate Editor of *Optics Express*.